Noninvasive Electrical Imaging of the Heart: Theory and Model Development

A. J. Pullan,[1] L. K. Cheng,[1] M. P. Nash,[2] C. P. Bradley,[2] and D. J. Paterson[2]

[1]Department of Engineering Science, The University of Auckland, Auckland, New Zealand and [2]University Laboratory of Physiology, University of Oxford, Oxford, United Kingdom

Abstract—The aim of this work is to begin quantifying the performance of a recently developed activation imaging algorithm of Huiskamp and Greensite [IEEE Trans. Biomed. Eng. 44:433–446]. We present here the modeling and computational issues associated with this process. First, we present a practical construction of the appropriate transfer matrix relating an activation sequence to body surface potentials from a general boundary value problem point of view. This approach makes explicit the role of different Green's functions and elucidates features (such as the anisotropic versus isotropic distinction) not readily apparent from alternative formulations. A new analytic solution is then developed to test the numerical implementation associated with the transfer matrix formulation presented here and convergence results for both potentials and normal currents are given. Next, details of the construction of a generic porcine model using a nontraditional data-fitting procedure are presented. The computational performance of this model is carefully examined to obtain a mesh of an appropriate resolution to use in inverse calculations. Finally, as a test of the entire approach, we illustrate the activation inverse procedure by reconstructing a known activation sequence from simulated data. For the example presented, which involved two ectopic focii with large amounts of Gaussian noise (100 μV rms) present in the torso signals, the reconstructed activation sequence had a similarity index of 0.880 when compared to the input source. © *2001 Biomedical Engineering Society.*
[DOI: 10.1114/1.1408921]

Keywords—Boundary element method, Critical point, Inverse problem of electrocardiography, Analytic solution, Activation sequence, Porcine model, ECG mapping, Body surface potentials.

INTRODUCTION

The goal of noninvasive electrical imaging of the heart is to quantitatively reconstruct information about the electrical activity of the heart from multiple thoracic ECG signals. Quantitative interpretation of these data in terms of the underlying cardiac electrical activity is an inverse problem and various mathematical algorithms have been developed over the years in an attempt to solve this electrical imaging problem.[1,16,20,25] Unless the problem is posed in a particular manner, this inverse problem is not uniquely determined, i.e., there exist multiple cardiac electrical generator configurations that can give rise to the same thoracic ECGs. This nonuniqueness has hampered attempts at solving the inverse problem. Early approaches to the inverse problem overcame the nonuniqueness by modeling the heart as a combination of a small number of fixed or moving dipoles. It has been recognized that posing the problem in terms of reconstructing epicardial potentials from the body surface potential recordings is uniquely determined. However, the reconstruction of epicardial potentials is ill-posed. This means that in the presence of noise (which always exists in practice), a solution to the inverse problem produces a result that may bear no resemblance to the true electrical generator. The emergence of a general theory for such ill-posed problems[32] and the introduction of the ideas behind constraining the mathematical solutions have resulted in the large number of inverse algorithms in existence today in the field of electrocardiac imaging. However, since many of the modern inverse ECG algorithms are based on such a general ill-posed inverse approach they fail to account for the underlying physiological processes governing the generation of the body surface potentials (namely, an evolving wave of activation). Moreover, many of the algorithms construct the inverse solution by treating each time instance independently, which, in theory at least, is not the optimal way to proceed with such temporally correlated information as is present in ECG signals.[14,15]

New Approach

Another approach to the inverse problem is to pose the problem in terms of the underlying activation sequence.[18] This has significant advantages over the epicardial potential problem formulation, not least in that it deals directly with the underlying physiological process responsible for generating the body surface potentials.

Address correspondence to Andrew Pullan, 6th Floor, 70 Symonds St., Department of Engineering Science, The University of Auckland, Private Bag 92019, Auckland, New Zealand. Electronic mail: a.pullan@auckland.ac.nz

However, it introduces additional difficulties in the modeling process, such as the need to model the entire heart instead of just modeling the epicardial surface (since myocardial activation times rather than just epicardial potentials are being related to body surface potentials). Also, it appears that activation-based imaging seems most suited for the ventricles and most relevant to the QRS interval only (although in principle it is possible to extend the approach beyond the QRS interval). As a result of this, and partly because of the fact that an appropriate algorithm for such a problem formulation had previously not been devised, this approach has not found much favor. However, a powerful new algorithm, based on this activation imaging approach has recently emerged.[14,17]

Both the epicardial and activation source formulations mentioned above have been recognized for 20 to 30 years, but as yet no clinically acceptable imaging techniques have resulted. The two major reasons for this are:

(1) Previously available mathematical methodologies for computation of the sources were not powerful enough.
(2) Adequate procedures for verification of the accuracy of the images were not employed.

For each of the two source formulations there are now powerful imaging algorithms that have not previously been available.[14,15,17] There are also sufficient modeling techniques now available that, when combined with these new algorithms, should make it possible to produce myocardial electrical source images of sufficient stability and accuracy to be a useful adjunct in the clinical assessment of the heart. However, these new algorithms need to be quantitatively validated before their clinical worth can be properly assessed.

In order to quantitatively validate the performance of the inverse procedures, one needs to compare any mathematical results against experimentally obtained *in vivo* data, in particular simultaneously recorded densely sampled body surface and cardiac potentials. This has rarely been attempted—rather the worth of various inverse procedures has often been judged by examining the performance on simulated data or in *in vitro* torso tank experiments. As far as is known until recently,[23] only two sets of *in vivo* data have ever been collected, one in a chimpanzee[31] (in which no inverse solution was attempted) and one in a dog.[1] Neither set is currently available. Data from *in vitro* experiments from perfused canine hearts in a homogeneous cylindrical tank have been collected by Taccardi *et al.* and are in use by that group and others.[25–27]

We present here the details of the underlying theory behind the electrical imaging process and the porcine model that we are using to validate this new inverse procedure. Some of this work has been communicated in abstract form.[3,21–23,29] We demonstrate the accuracy and convergence properties of the numerical procedure used to construct the transfer matrix. We also illustrate how the procedure is to be applied in practice by producing an inversely reconstructed cardiac surface activation map from simulated torso ECGs.

FORMULATION OF THE ACTIVATION INVERSE APPROACH

The basic activation inverse algorithm is presented in Huiskamp and Greensite.[17] The procedure revolves around the identification of the critical points and times of the surface activation function (i.e., epi- and endocardial breakthrough/termination points and times), via the use of a modified multiple signal classification algorithm. The use of this method on a given individual or animal requires the construction of an appropriate transfer function that maps the activation sequence to body surface potentials.

The proof of the activation imaging algorithm[14] uses source-field relationships,[34] which employ a Green's function that accounts for the anisotropy of the myocardium. While the new imaging algorithm proved from these relationships is completely general, the initial use of it has been restricted to using the so-called double-layer transfer matrices, which assume a homogeneous and isotropic myocardium. The traditional construction of such a double-layer transfer matrix begins with the assumption of myocardial homogeneity and isotropy and the use of equations defining the potential due to a dipole in free space.[8] We prefer to investigate the transfer matrix construction from a boundary value problem perspective (i.e., from solving the bidomain equations) that avoids explicit reference to dipoles. It also makes more explicit the anisotropic/isotropic distinction and elucidates features not apparent from a dipole formulation. This approach also generalizes some previously presented identities.[34] The full details of the construction of the transfer matrix from the bidomain equations is given in Appendix A.

The numerical discretization of the bidomain equations (inside the heart) and Poisson's equation (for passive tissue regions) results in an equation of the form [Eq. (45) of Appendix A]

$$
\begin{pmatrix} \text{coefficients} \\ \text{of potentials} \end{pmatrix}
\begin{pmatrix} \boldsymbol{\phi}_m \\ \boldsymbol{\phi}_e^H \\ \boldsymbol{\phi}^1 \\ \cdot \\ \cdot \\ \cdot \\ \boldsymbol{\phi}^N \end{pmatrix}
=
\begin{pmatrix} \text{coefficients} \\ \text{of currents} \end{pmatrix}
\begin{pmatrix} \mathbf{q}_e^H \\ \mathbf{q}^1 \\ \cdot \\ \cdot \\ \cdot \\ \mathbf{q}^N \end{pmatrix}, \quad (1)
$$

where

N is the number of tissue regions outside the heart,

$\boldsymbol{\phi}^i$ is a vector of nodal values of potential ϕ in region i,

$\boldsymbol{\phi}_m$ is a vector of nodal values of transmembrane potential ϕ_m on the heart,

$\boldsymbol{\phi}_e^H$ is a vector of nodal values of extracellular potential ϕ_e on the heart,

$\mathbf{q}^i$ is a vector of nodal values of current q on the surface of region i, and

$\mathbf{q}_e^H$ is a vector of nodal values of current q_e on the heart surface.

Equation (1) can be considered to be an implicit relationship between the vector of transmembrane potentials in the heart, $\boldsymbol{\phi}_m$, and the vector of torso potentials on the body surface, $\boldsymbol{\phi}_B$. To construct an explicit transfer matrix $\mathbf{T}_{BH}$, use is made of the definition of the transfer matrix, i.e.,

$$\boldsymbol{\phi}_B = \mathbf{T}_{BH}\boldsymbol{\phi}_m. \qquad (2)$$

Using this relationship, one simply needs to set $\boldsymbol{\phi}_m$ to be the vector $\mathbf{e}_k$ (i.e., a unit vector that is zero everywhere except at the kth position) and solve Eq. (1). The resulting solution for $\boldsymbol{\phi}_B$ will correspond to the kth column of $\mathbf{T}_{BH}$. Alternatively one can construct a transfer matrix from $\boldsymbol{\phi}_m$ to $\boldsymbol{\phi}_e^H$ by suitable rearrangement of Eq. (1).

No mention has yet been made of the nature of Eq. (1). The physical problem being solved suggests that Eq. (1) will be singular if $\boldsymbol{\phi}_m$ is the only variable to be specified, since no potential reference has been given. The system can either be solved in a least-squares sense or a technique such as deflation can be used.

The construction of the transfer matrix described in Appendix A has assumed homogeneity and isotropy in the heart muscle from Eq. (35) onwards. It is worth pointing out that the assumptions of homogeneity and isotropy are not required to use the activation imaging algorithm.[17] It is also possible to construct a transfer matrix relating activation times to torso potentials without these assumptions. However, the transfer matrix construction under anisotropic conditions becomes significantly more difficult. The bidomain equations [or a weak form of them, such as that given in Eq. (29) of Appendix A] have to be solved throughout the heart (using some volume-discretization procedure representing the full myocardial-fiber orientation) and coupled to solutions of Eq. (44) outside the heart. This dramatically increases the problem size. Work on this is progressing,[6] but at this stage homogeneity and isotropy are assumed.

Inverse Approximation to the Myocardial Activation Sequence

The activation inverse procedure that is used here has previously been described in detail.[17] Here, we include a summary of that method for completeness.

The basic idea behind the new approach stems from the observation that when an evolving cardiac activation wave front intersects the endocardial or epicardial surface a *hole* develops in the wave front. This is a significant change to the topology of the wave front and this change is reflected in the torso surface potential recordings. If $\tau(\mathbf{x})$ is defined to be the activation time on surface of the heart, Γ_H, at location $\mathbf{x}$, then these breakthrough points are critical points of $\tau(\mathbf{x})$, if the wave front breaks through at location $\mathbf{x}'$, then $\nabla\tau(\mathbf{x}')=0$ and $\tau(\mathbf{x}')$ is the time at which this breakthrough event occurs.

Following some considerable mathematical manipulation,[13] this critical point observation leads to two important results:

(1) $\mathbf{x}'$ is a critical point of $\tau(\mathbf{x})$ with critical time $\tau(\mathbf{x}')\Leftrightarrow\mathbf{t}_{BH}$ is in the space spanned by the spatial eigenvectors of $\boldsymbol{\phi}_B$, where $\mathbf{t}_{BH}$ is the column of the transfer matrix from $\boldsymbol{\phi}_m$ to $\boldsymbol{\phi}_B$ corresponding to the point $\mathbf{x}'$.

(2) With all critical points of $\tau(\mathbf{x})$ determined, the computation of $\tau(\mathbf{x})$ (on both the epicardial and endocardial surfaces) is a well-posed problem.

The key assumption required to prove the first point above is that $\phi_m(\mathbf{x},t)$ is modeled as a uniform step jump across the wave front, i.e.,

$$\phi_m^i(t,\boldsymbol{\tau}) = a + bH[t - \tau(\mathbf{x}^i)], \qquad (3)$$

where a represents the resting potential, b the height of the transmembrane potential jump, $H(\cdot)$ is the Heaviside step function, i is the index corresponding to the point $\mathbf{x}^i$ on the heart surface, and $\boldsymbol{\tau}=\{\tau^i\}=\tau(\mathbf{x}^i)$. [It should be noted that the notation in Eq. (3), and throughout this paper, is such that superscript indices indicated vector or matrix indices and subscripts indicate labels.]

This assumption is not a practical restriction for normal hearts. However, it does imply that the maximal temporal resolution is that of the duration of a transmembrane upstroke and the maximal spatial resolution is the width of the wave front (since below this resolution the activation wave front cannot be considered a step jump in space and time).

To compute the critical points and times, we require both the signal matrix $\Phi_{[1,S]}^{is}$ (of size $M \times S$, where M is the number of torso electrodes, S is the number of time samples, s is the sample number index, and j is the index corresponding to the point $\mathbf{y}^j$ on the torso surface) re-

corded from torso surface electrodes and the transfer matrix from $\boldsymbol{\phi}_m$ to $\boldsymbol{\phi}_B$, $\mathbf{T}_{BH}$. To determine the spatial (U) and temporal (V) eigenvector matrices of $\boldsymbol{\Phi}_{[1,s]}$, the singular value decomposition is used, i.e.,

$$\boldsymbol{\Phi}_{[1,s]} = \mathbf{U}_{[1,s]} \Sigma_{[1,s]} \mathbf{V}_{[1,s]}^T, \tag{4}$$

where $s \in [1,S]$.

The eigenvectors corresponding to *small* singular values are discarded, so the effective rank of U is R ($<M$). These discarded eigenvectors are assumed to represent only noise space.

In order to locate the critical points one needs to find the columns of $\mathbf{T}_{BH}$ that are contained in the space spanned by the spatial eigenvectors. A vector of reciprocal distances from signal space can be constructed by

$$M_{[1,s]}^i = \left(1 - \sum_{r=1}^{R} [\hat{\mathbf{t}}_{BH}^i \cdot \mathbf{u}_{[1,s]}^r]^2 \right)^{-1}, \tag{5}$$

where $\mathbf{u}_{[1,s]}^r$ is the rth column of the spatial eigenvector matrix $\mathbf{U}_{[1,s]}$ and $\hat{\mathbf{t}}_{BH}^i$ is the Euclidean normalized ith column of the transfer matrix $\mathbf{T}_{BH}$.

This distance measure greatly exaggerates points $\mathbf{x}$ which are close to signal space and is singular for points contained in this space. In practice, $M_{[1,S]}^i$ has no singularities since noise and errors associated with $\boldsymbol{\Phi}_{[1,S]}$ and $\mathbf{T}_{BH}$ ensure that no column of $\mathbf{T}_{BH}$ is contained exactly in signal space.

To find the activation times corresponding to these critical points, the following matrices are constructed:

$$M_+^{is} = M_{[1,s]}^i, \tag{6}$$

$$M_-^{is} = M_{[s,S]}^i, \tag{7}$$

where $1<s<S$. These two matrices examine the distance of each point from signal space, where the signal space is restricted to $[1,s]$ and $[s,S]$, respectively. For times (s) close to the activation time associated with each critical point $\mathbf{x}$, these matrices should undergo sharp changes, since $\mathbf{x}$ will begin to enter (leave) the signal space associated with the signal in time interval $[1,s]([s,S])$ as the signal space is enlarged (reduced).

The zero-crossing matrix, defined by

$$Z^{is} = M_+^{is} - M_-^{is}, \tag{8}$$

is theoretically zero at critical points of $\tau(\mathbf{x}^i)$ and has a steep gradient about these zeroes. In practice, the rows of Z^{is} contain numbers that increase from negative to posi-tive values and the time corresponding to the column index s of the number nearest zero provides an initial estimate of $\tau(\mathbf{x}^i)$.

Activation Sequence Optimization

With all critical points and times identified, the next step is to determine $\tau(\mathbf{x})$ on the heart surfaces. This theoretically well-posed process is formulated as an optimization problem, where the objective is to minimize the difference between calculated torso potentials and the measured potentials. Additional constraints on the optimization process can be imposed, e.g., addition of the surface Laplacian of the $\tau(\mathbf{x})$ to the minimization.[18] The use of ϕ_m^i in Eq. (3) gives rise to a residual that is not continuous with τ. From an optimization point of view, it is more desirable to be dealing with functions which are continuous. Moreover, the speed of convergence is greatly aided by continuous derivatives. Thus, one typically modifies Eq. (3) so that ϕ_m^i has a sharp but continuous upstroke duration as in, e.g., a generalized form of the activation function[18]

$\phi_m^i(t, \mathbf{u}, \tau)$

$$= \begin{cases} u^1 & t - \tau^i \leq \dfrac{-u^3}{2} \\[2mm] u^1 + \dfrac{u^2}{2}\left(\dfrac{2(t-\tau^i)}{u^3} + 1 \right)^2 & \dfrac{-u^3}{2} < t - \tau^i \leq 0 \\[2mm] u^1 + u^2 - \dfrac{u^2}{2}\left(\dfrac{2(t-\tau^i)}{u^3} - 1 \right)^2 & 0 < t - \tau^i < \dfrac{u^3}{2} \\[2mm] u^1 + u^2 & t - \tau^i \geq \dfrac{u^3}{2}, \end{cases}$$

$$\tag{9}$$

where u^1 is the resting potential, u^2 is magnitude of the transmembrane potential jump, u^3 is the duration of the action potential upstroke, and $\mathbf{u} = \{u^k\}$ is the vector of parameters defining the activation wave function.

The final objective function, which is minimized by adjusting activation times, is

$$\min F(\tau, \mathbf{u}) = \mathbf{f}^T(\tau, \mathbf{u})\mathbf{f}(\tau, \mathbf{u}) + \lambda \mathcal{L}[\tau(\mathbf{x})], \tag{10}$$

where $\mathcal{L}$ is the Laplacian of the activation field and λ is a parameter that controls the degree of regularization imposed on the objective function.

There are a number of choices for the residual vector $\mathbf{f}(\tau, \mathbf{u})$ in the optimization problem. A common choice is to set the residual to be

$$f^j(\tau, \mathbf{u}) = \| \boldsymbol{\phi}_B^i - \hat{\boldsymbol{\phi}}_B^j(\tau, \mathbf{u}) \|_2, \tag{11}$$
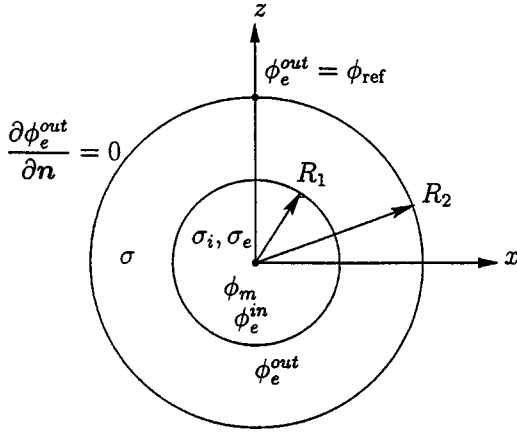
FIGURE 1. Schematic of analytic problem setup, with inner sphere of radius R_1 and outer sphere of radius R_2. Conductivity parameters of σ_i and σ_e in the inner sphere and σ in the outer sphere were specified. The transmembrane potential ϕ_m on the inner surface is specified by Eq. (47) and a no-flux boundary condition is specified on the outer surface. The extracellular potential, ϕ_e^{in}, on the inner surface and ϕ_e^{out} on the outer surface and the normal derivatives were computed.

where $\boldsymbol{\phi}_B^j$ is the jth row of the matrix of known body surface potentials $\mathbf{\Phi}_B = \mathbf{\Phi}_{[1,S]}$ and $\hat{\boldsymbol{\phi}}_B^j(\boldsymbol{\tau},\mathbf{u})$ is the jth row of the matrix of calculated body surface potentials, $\hat{\mathbf{\Phi}}_B(\boldsymbol{\tau},\mathbf{u})$, given by

$$\hat{\Phi}_B^{is}(\boldsymbol{\tau},\mathbf{u}) = T_{BH}^{ji} \phi_m^i(t^s,\boldsymbol{\tau},\mathbf{u}), \qquad (12)$$

where $s \in [1,S]$ and t^s is the actual time at which the sth sample was recorded.

The critical points can be constrained in several different ways, e.g., the critical points and times could be fixed, or the critical points could be constrained to remain local maxima or minima of $\tau(\mathbf{x})$. However, imposing such constraints is of questionable practical value at this stage. The reason for this is that it is not always clear which points, in the presence of geometric noise, are true critical points and hence the choice of which points to constrain can be subjective. Thus, optimizations are typically performed with no constraints on the critical points. It is also possible to optimize on the upstroke duration u^3 as well as the voltages u^1 and u^2, although these are typically fixed before optimization begins.

As with almost all inverse methods, the above requires an appropriate forward transfer matrix $\mathbf{T}_{BH}$ that has been carefully validated. This is the focus of the following section.

FORWARD MODEL VALIDATION

To verify the accuracy of the numerical solution process used to construct and solve Eq. (45) in Appendix A, we present here results for a simplified case for which an analytic solution can be constructed.

Test Problem

Two concentric spheres (as shown in Fig. 1) were constructed, with the inner and outer spheres representing the epicardial and torso surfaces, respectively. A spherical-polar coordinate system (r, θ, ζ), with $0 \leq \theta < 2\pi$ for the circumferential coordinate and $0 \leq \zeta \leq \pi$ for the azimuthal coordinate, was used to geometrically describe and analytically solve the problem, although numerical solutions were carried out in a rectangular Cartesian framework.

The extracellular potential was denoted by ϕ_e^{in} and ϕ_e^{out} for the inner and outer spheres, respectively.

The governing equations and boundary conditions of this problem closely mimic that of the true problem. We ultimately wish to deal with the problem that is governed by Eqs. (24) and (44) in Appendix A and subject to the boundary conditions [Eqs. (13)–(17)].

A reference potential ϕ_{ref} was set at the top of the outer sphere $(R_2, \theta, 0)$ as specified by Eq. (17):

$$\frac{\partial \phi_m}{\partial \tau} = 0 \quad \text{at } r = R_1, \qquad (13)$$

$$\phi_e^{\text{out}} = \phi_e^{\text{in}} \quad \text{at } r = R_1, \qquad (14)$$

$$(\sigma_i + \sigma_e) \frac{\partial \phi_e^{\text{in}}}{\partial r} = \sigma \frac{\partial \phi_e^{\text{out}}}{\partial r} \quad \text{at } r = R_1, \qquad (15)$$

$$\frac{\partial \phi_e^{\text{out}}}{\partial r} = 0 \quad \text{at } r = R_2, \qquad (16)$$

$$\phi_e^{\text{out}} = \phi_{\text{ref}} \quad \text{at } r = R_2, \zeta = 0. \qquad (17)$$

We chose ϕ_m to be the potential that would be set up by a dipole $\boldsymbol{\rho}$ inside a sphere of radius R_1. This choice satisfies Eq. (13) and ensures a nontrivial solution can be obtained. With the use of associated Legendre polynomi-

als, analytic expressions for the extracellular potentials on both surfaces can be calculated. The derivation of the general solution to the above is given in Appendix B.

A particular solution for this general case is also given in Appendix B. With $R_1 = 1$ and $R_2 = 3$, the dipole speci-

fied by $\boldsymbol{\rho} = (1,2,1)$, the bidomain conductivities given by $\sigma_i = 2$ and $\sigma_e = 4$, the passive conductivity set to $\sigma = 2$, and four of the coefficients of the general solution taken as $C_{11} = 1$, $D_{11} = 1$, $D_{11} = 1$, and $C_1 = 1$, the particular solution in this case is

$$
\phi_e = \begin{cases}
\left(\dfrac{52}{17}\cos\theta + \dfrac{104}{17}\sin\theta \right)\left(r + \dfrac{1}{r^2} \right)\sin\zeta + \left(r + \dfrac{87}{122r^2} \right)\cos\zeta - \dfrac{27}{122} \\[2mm]
\qquad - \dfrac{(2r^3+1)}{3r^2}(\cos\theta\sin\zeta + 2\sin\theta\sin\zeta + \cos\zeta) \qquad\qquad 0 < r \leqslant 1 \\[3mm]
\left(\dfrac{81}{17}\cos\theta + \dfrac{162}{17}\sin\theta \right)\left(\dfrac{2r}{27} + \dfrac{1}{r^2} \right)\sin\zeta + \left(\dfrac{3r}{61} + \dfrac{81}{122r^2} \right)\cos\zeta - \dfrac{27}{122} \quad 1 < r \leqslant 3,
\end{cases}
\tag{18}
$$

and the radial derivatives given by

$$
\frac{\partial \phi_e}{\partial r} = \begin{cases}
\left(\dfrac{52}{17}\cos\theta + \dfrac{104}{17}\sin\theta \right)\left(1 - \dfrac{2}{r^3} \right)\sin\zeta + \left(1 - \dfrac{174}{122r^3} \right)\cos\zeta \\[2mm]
\qquad - \dfrac{2(r^3-1)}{3r^3}(\cos\theta\sin\zeta + 2\sin\theta\sin\zeta + \cos\zeta) \qquad\qquad 0 < r \leqslant 1 \\[3mm]
\left(\dfrac{81}{17}\cos\theta + \dfrac{162}{17}\sin\theta \right)\left(\dfrac{2}{27} - \dfrac{2}{r^3} \right)\sin\zeta + \left(\dfrac{3}{61} - \dfrac{162}{122r^3} \right)\cos\zeta \quad 1 < r \leqslant 3.
\end{cases}
\tag{19}
$$

The numerical solutions for varying mesh refinements were compared to analytically generated solutions as specified by Eqs. (18) and (19). Equation (20) provides a direct comparison between the analytic and numerical solutions while Eq. (21) provides a relative percentage comparison between the two solutions. If we denote the goal potential (or current) field at node i as ϕ^i and the computed potential (or current) field at the same point as $\hat{\phi}^i$, the root-mean-square (rms) error is given by

$$
\text{rms} = \sqrt{\frac{\sum\limits_{i=1}^{N}(\phi^i - \hat{\phi}^i)^2}{N}},
\tag{20}
$$

and the normalized integral difference squared (NIDS) is given by

$$
\text{NIDS} \ (\%) = \sqrt{\frac{\int_\Gamma (\phi(\mathbf{x}) - \hat{\phi}(\mathbf{x}))^2 d\Gamma(\mathbf{x})}{\int_\Gamma \phi(\mathbf{x})^2 d\Gamma(\mathbf{x})}} \times 100\%.
\tag{21}
$$

The problem was solved using bilinear basis functions with the mesh systematically refined in each coordinate direction. The convergence plots for potentials and cur-

rents on both surfaces are shown in Figs. 2 and 3, respectively. The error measures are plotted against the average characteristic element size (square root of the average of the areas of each element), h, and the solution degrees of freedom (DOF). The slopes of the NIDS lines in Figs. 2 and 3 are 2.7 and 2.5, respectively, and thus the problem has a linear convergence rate of at least $O(h^2)$.

Figure 4 shows the potential and the current values at five evenly spaced points, determined by setting $\theta = 0$ and varying ζ from 0 to π. Effectively, this is a slice from the top to the bottom of the sphere from the lowest-resolution mesh, which allowed the solution fields at different refinement levels to be compared. The plot on the left shows the potential on the outer surface ($r = R_2$) and the plot on the right the current at the inner surface ($r = R_1$). Note that the reference potential is set to 0 mV at $\zeta = 0$ on the outer surface and the no-flux boundary condition ensures that the current is always zero at $r = R_2$.

Reassuringly, as the mesh was refined, the solution approached the analytic solution and the numerical implementation of the transfer matrix was validated. This allowed us to confidently proceed towards the construc-
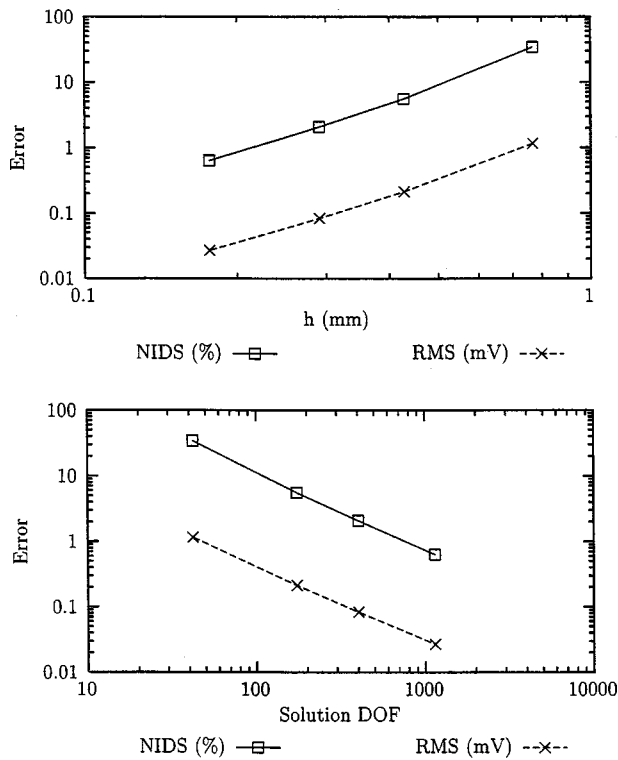
FIGURE 2. Convergence analysis for the extracellular potential on the surface of both spheres for the analytic test problem. Shown are the two error measures defined in Eqs. (20) and (21) as functions of mesh refinement (h) and solution matrix size (solution degrees of freedom).
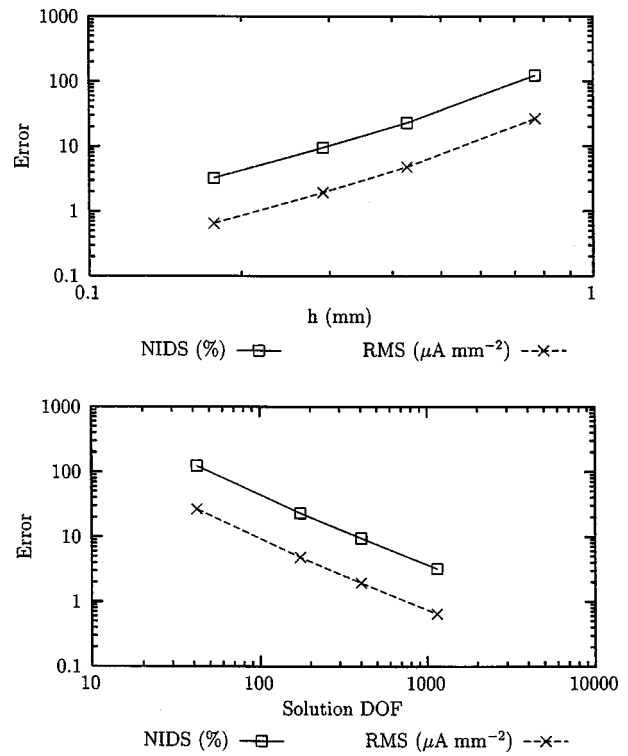

FIGURE 3. Convergence analysis for the normal current flow through the inner sphere surface for the analytic test problem. Shown are the two error measures defined in Eqs. (20) and (21) as functions of mesh refinement (h) and solution matrix size (solution degrees of freedom).

tion and validation of a porcine model to be used to investigate the new inverse algorithm.

PORCINE MODEL DEVELOPMENT

The geometric organization of the torso and its constituents are of central importance to the ECG inverse algorithms described in the section on formulation of the activation inverse approach. This is primarily due to the calculation of the transfer matrix, which relates heart transmembrane potentials to torso potentials. Our ultimate aim is to validate ECG inverse algorithms using *in vivo* data obtained from pigs. To achieve this, a computational model of a pig is required. To construct our generic pig model, we obtained a sequence of cross-sectional CT torso images from a young 20 kg pig that was artificially ventilated. Each CT image was acquired with the lungs fully inflated.

Images were digitized to provide a three-dimensional data set of the endocardial, epicardial, lung, fat, and skin surfaces. These data were then used with a previously developed nonlinear optimization procedure that incorporates nonlinear constraints and smoothing[4] to obtain a parametric representation (based on C^1 cubic Hermite

elements) of the above surfaces. Such a representation allows for the construction of an efficient, anatomically accurate computational model of the pig.

A summary of the results achieved from this fitting procedure using the porcine data is given in Table 1. The fitted porcine model is shown in Fig. 5. Due to the leanness of the young pig, the fat layer was not explicitly modeled. This generic model is referred to later as the model with level 0 refinement (see Table 3) and provides a framework on which to validate certain aspects of the whole procedure (e.g., the appropriate mesh resolution to use in the computational forward model). Customization of this generic pig model for a given pig experiment has been previously described.[7,22,23]

ANALYSIS OF MODEL CONVERGENCE USING FORWARD CALCULATIONS

The model discretization process introduces numerical approximation errors into the solution procedure. By refining the mesh, and thereby increasing the number of solution degrees of freedom, the error associated with the discretization process generally decreases. Once the
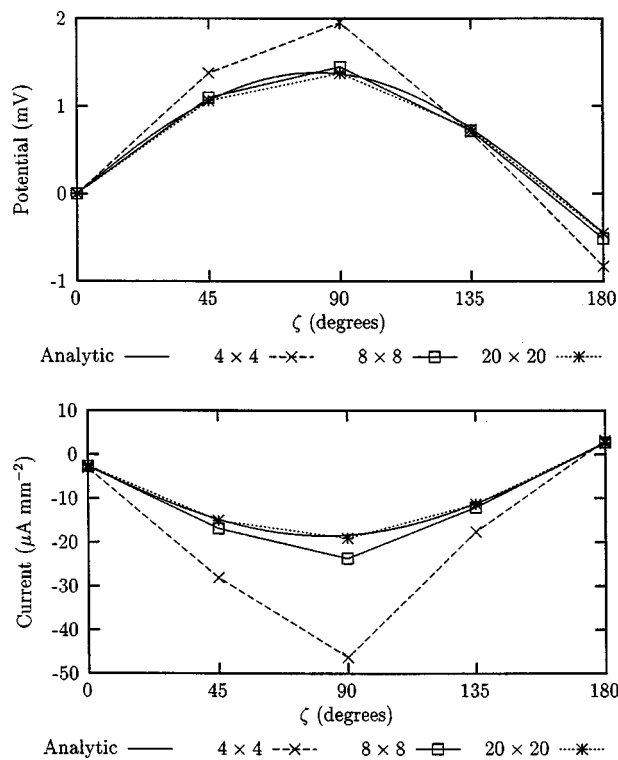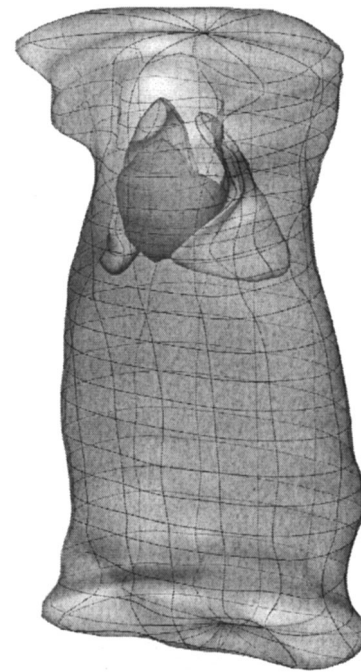
FIGURE 4. Comparison between the analytic and the numerical extracellular potentials at $r = R_2$ and the currents at $r = R_1$ for the analytic test problem.

FIGURE 5. Anatomically accurate model of the porcine torso, showing the outer skin layer, lungs, and heart from an anterior perspective. Dark lines show the smoothly continuous elements of the lowest resolution computational mesh.

mesh has been refined to a point where the change in solution is less than an acceptable tolerance, the solution is said to have converged.

In order to use the inverse ECG algorithm to confidently quantify electrocardiac activity, the effects on the results of computational mesh resolution must be investigated *a priori*. This section presents an analysis of the solution convergence based on forward ECG calculations, for which torso potentials were computed using a prespecified electrocardiac source together with the transfer matrix for the computational model.

TABLE 1. Summary of the results obtained by fitting piecewise bicubic Hermite surfaces to digitized CT slices of a particular pig. The rms errors compare digitized data points to their orthogonal projections onto the fitted surfaces.

Surface	Number of data points	rms error (mm)
Epicardial	1603	1.23
Left ventricle	500	1.47
Right ventricle	892	1.13
Left lung	2011	2.14
Right lung	2640	2.71
Outer torso	2417	2.47
Average rms		1.86

Electrocardiac Sources

To solve the forward problem of electrocardiology, a cardiac source that specifies the electrical distribution of the myocardium is required. This source may either be recorded by invasive means, approximated using electrical models of the myocardium, or approximated using recordings from sources thought to represent the epicardial potential distribution from a heart inside a torso. For our convergence analysis, two different cardiac sources were used.

The first was a simple dipole source with a fixed center and varying magnitude and direction. The direction was specified for 300 times steps at time intervals of 2 ms.[2] The use of such a source allows one to investigate the mesh resolution necessary for a converged epicardial potential to body surface potential forward problem—a necessary prerequisite before attempting a traditional epicardial potential inverse procedure. While such an inverse is not the aim of the present work, it is assumed that this analysis will provide valuable insight into the mesh resolution required for accurate activation inverse reconstructions.

The second source was a surface activation profile. This was derived from an activation map obtained using an eikonal model of cardiac activation[33] and solved on a finite-element model of the canine heart.[19,24] The resulting activation profile produced by the eikonal model on the canine heart was then transformed to the geometry of
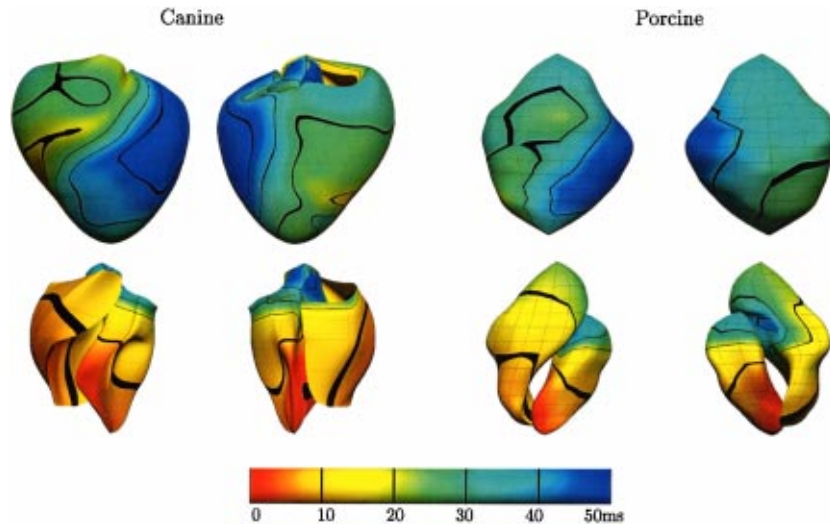
FIGURE 6. Epicardial surfaces (top row) and ventricular chambers (bottom row), with activation profiles displayed as a color field, shown from anterior and posterior views. The activation profile of the canine ventricles (left two columns) was fitted to the epicardial and endocardial surfaces of the porcine model (right two columns), which resulted in an activation range of 0−52 ms compared with 0−55 ms for the canine heart. The canine activation was generated from an eikonal model (see Ref. 33) with experimentally determined endocardial activation times used as boundary conditions. The porcine activation sequence was one of the heart sources used in the convergence analysis.

the porcine heart model by projecting nodal values orthogonally onto the surface of the porcine heart and fitting the field using least squares. This resulted in slightly different activation times on the two geometrically different meshes. The original canine activation profile and the fitted porcine profile are illustrated in Fig. 6. The activation field of the canine model has a range of 0–55 ms, while the porcine model has a range of 0–52 ms.

Material Properties

The material conductivities used for this study were derived from a number of papers[10,11,30] and were chosen to be consistent with those of other torso models in the literature.[5,9] A summary of the conductivity values used for the forward analysis is given in Table 2. Since activation sequences have been shown to be virtually independent of the surrounding torso conductivity,[12] the exact values of the conductivities are thought to be of minimal

importance to our proposed inverse studies. This is in contrast to the epicardial potentials approach, which can change dramatically with surrounding tissue impedance.[12] No attempt has been made to measure the conductivities of various organs during the porcine experiments and we have chosen to use the values in Table 2 in our inverse analysis.

Comparison Methodology

To compare the effect of model refinement, a number of metrics were used to quantify the differences between a particular result from two different simulations. Given the temporal and spatial nature of each solution set, the data were reduced by comparing the potential distribution over a subset of nodes at a fixed time. In addition to Eqs. (22) and (23), the maximum and minimum potentials were also compared.

Table 3 shows mesh statistics at the generic and the converged refinement level for each surface of the model. The initial level of refinement (level 0) refers to the mesh resolution achieved from the geometric fitting. Each level of refinement involved refining the surfaces once in each of the two parametric (ξ) directions. The epicardium was refined an additional time in the circumferential (ξ_1) direction to achieve a refinement level of 2.5. Two measures were used to characterize the level for refinement of each surface. These were the number of degrees of freedom (which is directly related to the order of the basis function and the number of nodes) and a characteristic element size (denoted h). The characteristic

TABLE 2. Material conductivities used for the porcine model. Values were sourced from experimental papers (see Refs. 10, 11, and 30) and other torso models (see Refs. 5 and 9).

Tissue	Resistivity (Ω cm)	Conductivity (mS mm^{-1})	Ratio to torso cavity
Blood	159	0.63	2.86
Intracellular	333	0.30	1.36
Extracellular	333	0.30	1.36
Lungs	2000	0.05	0.23
Torso	255	0.22	1.00

TABLE 3. Mesh statistics for each surface of the generic porcine model. Each surface has the refinement level required for a geometrically accurate mesh (level 0) and the refinement level required for a computationally converged solution. Refinement level 0 refers to the surfaces created from geometric fitting. Each additional level of refinement involves refining the surface uniformly in each of the parametric (ξ) directions.

Surface	Refinement level	Nodes	Elements	Geometric DOF per coordinate	Characteristic element size h (mm)
Epicardium	0	37	40	142	21.3
	1	152	160	602	10.6
	2	622	640	2658	5.3
Left lung	0	74	80	290	17.9
	1	306	320	1218	8.9
Right lung	0	74	80	290	20.4
	1	306	320	1218	10.2
Left ventricle	0	27	30	102	13.0
	1	112	120	442	7.0
Right ventricle	0	38	42	146	14.8
	1	158	168	626	7.4
Skin	0	254	264	1010	37.3
	1	1034	1056	4130	18.6

element size was defined to be the square root of the average element area.

We use two main metrics to quantify the difference between a master signal matrix ($\mathbf{\Phi}_B$) and a comparison signal matrix ($\hat{\mathbf{\Phi}}_B$). The first metric is the similarity index (SI), or correlation coefficient, which is independent of the magnitude of the two signals. It quantifies the linear relationship between two variables and is insensitive to scaling or translation in the magnitudes of the vectors with respect to one another. The SI thus provides a measure of the degree to which the spatiotemporal topography of the fields differ between two samples. The second metric is the relative root-mean-squared error (relative rms), which quantifies the difference in the magnitude between two fields. It is sensitive to a scaling or translation in the magnitudes of one vector with respect to another.

The similarity index is defined as

$$
\text{similarity index}
= \frac{\boldsymbol{\phi}_B^k \cdot \hat{\boldsymbol{\phi}}_B^k - \dfrac{(\boldsymbol{\phi}_B^k \cdot \mathbf{e})(\hat{\boldsymbol{\phi}}_B^k \cdot \mathbf{e})}{\|\mathbf{e}\|_2^2}}{\sqrt{\left(\boldsymbol{\phi}_B^k \cdot \boldsymbol{\phi}_B^k - \dfrac{(\boldsymbol{\phi}_B^k \cdot \mathbf{e})^2}{\|\mathbf{e}\|_2^2}\right)\left(\hat{\boldsymbol{\phi}}_B^k \cdot \hat{\boldsymbol{\phi}}_B^k - \dfrac{(\hat{\boldsymbol{\phi}}_B^k \cdot \mathbf{e})^2}{\|\mathbf{e}\|_2^2}\right)}},
$$
(22)

and the relative root-mean-squared error is defined as

$$
\text{relative rms} = \frac{\|\boldsymbol{\phi}_B^k - \hat{\boldsymbol{\phi}}_B^k\|_2}{\|\boldsymbol{\phi}_B^k\|_2},
$$
(23)

where, for a similarity index or relative rms at a fixed sample (or fixed point on the torso), $\boldsymbol{\phi}_B^k$ is the kth column (row) of the $\mathbf{\Phi}_B$ matrix, $\hat{\boldsymbol{\phi}}_B^k$ is the kth column (row) of the $\hat{\mathbf{\Phi}}_B$ matrix, and $\mathbf{e}$ is the $M \times 1$ ($1 \times S$) vector of ones.

In addition to the two main error metrics, the magnitudes of the maxima and minima potential values were also compared between different solution fields. This error metric can be extremely sensitive to changes between the fields as they simply compare a single potential value, while the relative rms and SI compare the fields as a whole. As the fields were compared at the relative sparse nodal locations of the lowest-resolution model, changes in the locations of the maxima and minima potentials were not considered.

Convergence Analysis With The Moving Dipole Source

Using the dipole source specified in the section on electrocardiac sources, a range of simulations at different refinement levels was performed to quantify the effect of varying the mesh resolution on solution convergence.

TABLE 4. Effect of refining the epicardial surface on the torso surface potentials using a moving dipole source. All regions, apart from the epicardium, were maintained at the refinement level set by the reference model (both lungs and torso surface at level 1 refinement). The various comparison metrics are listed in the first column. The second column outlines the different levels of refinement used for each surface, while the remaining columns show the comparisons at different time instances. Level 2.5 corresponds to refining the level 2 mesh in just the circumferential direction.

Measure	Epicardial refinement level	Peak P	Peak R	Peak T	QRS integral
	0–1	0.032	0.047	0.105	0.041
Rel. rms	1–2	0.001	0.003	0.003	0.002
	2–2.5	0.001	0.001	0.003	0.002
	0–1	1.000	0.999	0.997	0.999
SI	1–2	1.000	1.000	1.000	1.000
	2–2.5	1.000	1.000	1.000	1.000
	0–1	10.39	14.33	−12.00	8.15
Max. $\Delta\phi\%$	1–2	−0.07	−0.09	0.28	−0.04
	2–2.5	0.22	0.07	0.06	0.06
	0–1	0.56	0.90	−8.42	−0.10
Min. $\Delta\phi\%$	1–2	0.09	−0.02	0.28	0.00
	2–2.5	0.04	0.01	0.09	0.02

To quantify the changes between refined meshes, the potentials at the nodal positions from the least-refined case (level 0) were used to compute the error measures. There were 37 sites on the epicardium and 254 sites on the torso surface used for the comparisons.

Key events in the cardiac cycle were used as temporal markers for comparisons. They were peak P at 115 ms, peak R at 240 ms, and peak T at 505 ms. The QRS interval was considered to span 190–290 ms. These times were determined by solving the forward problem and examining the resultant signals on the dominant chest leads.

Since the use of the dipole source was to determine the appropriate mesh resolution for a traditional potential inverse, no blood masses were included in the forward simulations involving this source. An isoparametric formulation was used in the forward solutions, i.e., the dependent variable (potential) was approximated using the same basis functions as used to approximate the geometry (cubic Hermite interpolation). Epicardial potentials were calculated from the dipole source inside the heart as part of the solution process and these potentials changed with heart mesh refinement. Therefore, for this analysis, both epicardial and torso surface potentials were compared.

To test whether a model with a certain refinement level had converged, a particular region was progressively refined until there was no significant change in the solution. To determine the appropriate resolution of the entire mesh, this process was repeated with the other regions in the mesh at various levels of refinements.

From this large number of simulations, a reference model, which had each region at an appropriate resolution for a converged forward solution, was chosen. This reference model contained the epicardium refined to level 2, the left and right lung to level 1, and the torso to level 1 refinement.

To illustrate the process, Table 4 summarizes the effect that epicardial surface refinement had on the resulting torso potentials. In this case, a level 1 refinement of the epicardium produced a converged solution. Other simulations show that the epicardial potentials themselves did not converge until the epicardium was refined to level 2. The average element length for the refined model was 5.3 mm on the heart. This model resulted from a double refinement for the heart (from 40 to 640 elements) and single refinements for the lungs (from 80 to 320 elements) and torso (from 264 to 1056 elements).

Convergence Analysis With Activation Sequence Source

The process described in the previous section was repeated using the activation profile specified in the section on electrocardiac sources.

Since the activation sequence was derived from an eikonal solution on a ventricular heart model,[33] just the QRS interval of the cardiac cycle was considered. As outlined in the section on electrocardiac sources, the activation sequence progressed for a total of 52 ms. Key events of the QRS interval were used as temporal markers for comparisons. They were peak Q at 12 ms, peak R at 31 ms, and peak S at 43 ms. The QRS interval

TABLE 5. Effect of refining the epicardial surface on the torso potentials using an activation source. All regions, apart from the epicardial surface, were maintained at the refinement level for the reference model (left and right ventricular chambers, both lungs, and torso surfaces at level 1). The column layout is the same as Table 4.

Measure	Epicardial refinement level	Peak P	Peak R	Peak T	QRS Integral
Rel. rms	0–1	0.071	0.298	0.250	0.057
	1–2	0.014	0.058	0.131	0.036
	2–2.5	0.002	0.009	0.032	0.006
SI	0–1	0.997	0.938	0.989	0.998
	1–2	1.000	0.998	0.994	1.000
	2–2.5	1.000	1.000	1.000	1.000
Max. $\Delta\phi\%$	0–1	−14.67	−1.88	−26.56	−12.55
	1–2	−1.81	−3.10	−3.96	−0.87
	2–2.5	0.12	0.81	1.37	1.35
Min. $\Delta\phi\%$	0–1	3.08	44.42	3.38	−1.02
	1–2	0.42	16.98	−1.02	−1.97
	2–2.5	0.05	−0.25	2.65	0.39

spanned 0–52 ms. These times were again determined by solving the forward problem and examining the resultant signals on the torso surface.

The use of a prescribed activation sequence meant that refinement of the myocardial surfaces had no effect on the resulting activation times, since they were simply interpolated from the unrefined model, as illustrated in Fig. 6. This is in contrast to the moving dipole source, for which the epicardial potentials were calculated as part of the solution process.

Following the section on convergence analysis with the moving dipole source, the changes between refined meshes were quantified using just the potentials at the nodal positions on the torso surface of the unrefined model (254 sites). Again, convergence was determined by altering the refinement level of a given region, while holding all other regions constant. Table 5 summarizes the effect of epicardial surface refinement on computed torso potentials. To obtain converged solutions using the activation source, one refinement in each ξ direction was needed for each surface.

Summary of Convergence Analysis

In summary, Table 3 details the statistics for each level of refinement for each surface. For the activation heart source, convergence was achieved using a level 1 refinement of all surfaces. The moving dipole heart source required a level 2 refinement for the epicardial surface and level 1 refinements for the lungs and outer torso. Thus, this model was selected for the simulations in the next section, which illustrate the inverse procedure.

ACTIVATION RECONSTRUCTIONS USING THE PORCINE MODEL

To illustrate the activation inverse approach using a realistic pig geometry, we present here results using simulated data. A known activation profile was generated by specifying a number of initial activation sites (shown as purple spheres in Fig. 7). Activation times were then generated for all points on the heart surfaces based on the distance to the nearest activation site (which is equivalent to solving a simple activation model in a homogeneous heart).

Given this *goal* activation profile, torso surface potentials were generated by solving Eq. (45). This resulted in potentials at all points on the torso surface in the absolute range of 0–4 mV. Gaussian noise with an absolute magnitude of 100 μV rms was added to these torso surface signals and used as input for the inverse procedure. This is somewhat larger than one would typically encounter in a clinical setting, but is used here to provide a stern test of the inverse process. At this stage no geometric or correlated noise had been added to the system.

The transfer matrix used to generate this map consisted of 1034 rows and 422 columns. The upper and lower bounds of each activation time was set to 0 and 100 ms, as defined by the activation sequence and the body surface potentials. A sigmoidal activation function[18] was used to represent the action potential. The magnitude of the transmembrane jump of Eq. (9) was fixed at 100 mV and the width of the upstroke duration was 5 ms.

A series of simulations were performed, with various for the regularization parameter (λ) in Eq. (10). The
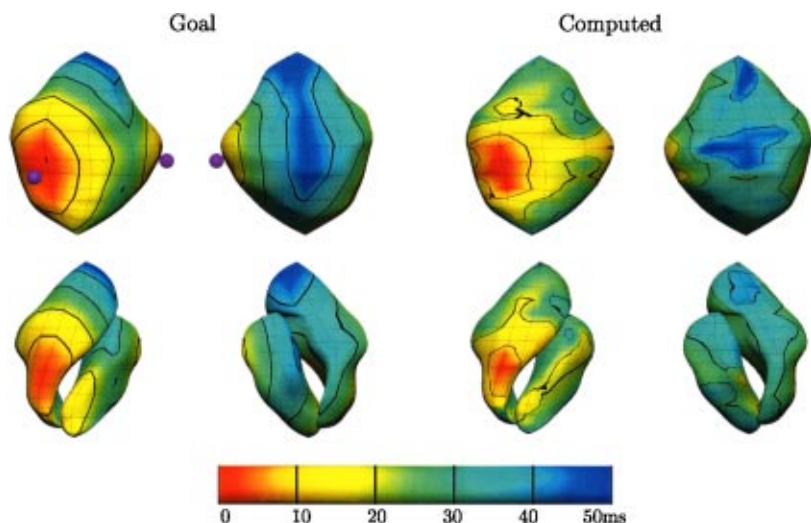
FIGURE 7. Goal and computed activation fields displayed on the epicardial and endocardial surfaces (layout as described in Fig. 6). The goal activation map is shown on the left two columns and the computed activation map on the right two columns. Dark purple spheres represent the initial seed points used to generate the activation sequence.

computed activation field was found to be fairly insensitive to the amount of regularization. Theoretically, with the critical points and times accurately defined, the problem becomes well posed. However, in practice, the zero-crossing algorithm is only able to provide an estimation of the critical point locations and their corresponding times. With high levels of regularization, smoother activation fields resulted. However, this did not necessarily result in an improved inverse solution. The maxima and minima tended to be damped out, resulting in a poorer, but smoother activation field.

A comparison between the measured and calculated activation maps is given in Fig. 7. The measured and reconstructed activation profiles are shown on the left and right pairs of epicardial surfaces, respectively. The goal activation sequence had a range of 24–74 ms with a duration of 50 ms. The inversely reconstructed activation sequence ranged from 24 to 75 ms with a duration of 51 ms. The goal and computed body surface potentials and activation sequences were compared using the metrics defined in Eqs. (22) and (20). The goal and computed body surface signals had a rms error of 0.94 mV and a SI of 0.998. The relative rms error between the goal and computed activation times was 5.6 ms, while the SI was 0.880 and the maximum error was 17.8 ms. Thus, the activation inverse approach successfully reconstructed the electrocardic source.

CONCLUSIONS

We have presented the theoretical issues associated with quantitatively reconstructing activation sequences from densely sampled thoracic ECG signals. The ultimate aim of this work is to begin assessing new activation imaging algorithms[18] using *in vivo* data acquired from pigs.

We have discussed in some detail the solution of the governing equations, including a practical generalization of some previously published identities.[34] We have described the process used to construct the porcine model from CT images. A careful convergence analysis of the forward problem was conducted in order to provide a model with an appropriate resolution for the inverse problem.

A new analytic solution was derived for a spherical geometry and this was used to illustrate the accuracy and convergence properties of the numerical procedure used in the transfer matrix construction. The numerical solutions converged to the analytic solutions in a linear fashion.

Finally, the inverse process was illustrated by reconstructing the activation sequence using simulated data with a porcine model. With Gaussian noise of 100 μV and no geometric noise, the resulting activation sequence was successfully reconstructed.

APPENDIX A: TRANSFER MATRICES FROM A BOUNDARY VALUE PROBLEM PERSPECTIVE

Let Ω_H be the domain of the heart, $\Gamma_H = \partial\Omega_H$ (the closed surface of the heart), ϕ_i the intracellular potential, ϕ_e the extracellular potential, $\phi_m = \phi_i - \phi_e$ the transmembrane potential, and $\boldsymbol{\sigma}_i$ and $\boldsymbol{\sigma}_e$ the intracellular and extracellular conductivity tensors, respectively.

From bidomain theory, inside Ω_H we have

$$\nabla \cdot ([\boldsymbol{\sigma}_i + \boldsymbol{\sigma}_e]\nabla\phi_e) = -\nabla \cdot (\boldsymbol{\sigma}_i \nabla \phi_m). \qquad (24)$$

This is a Poisson equation for ϕ_e in which the source term is the right-hand side of Eq. (24).

One can solve this partial differential equation using a weighted residuals approach. Let w be a (yet unspecified) weighting function. From weighted residuals we then have

$$\int_{\Omega_H} \nabla \cdot ([\boldsymbol{\sigma}_i + \boldsymbol{\sigma}_e]\nabla\phi_e)w\,d\Omega + \int_{\Omega_H} \nabla \cdot (\boldsymbol{\sigma}_i \nabla \phi_m)w\,d\Omega = 0. \qquad (25)$$

Using Green's theorem, we get

$$\int_{\Gamma_H} w[\boldsymbol{\sigma}_i + \boldsymbol{\sigma}_e]\nabla\phi_e \cdot \mathbf{n}\,d\Gamma - \int_{\Omega_H} [\boldsymbol{\sigma}_i + \boldsymbol{\sigma}_e]\nabla\phi_e \nabla w \cdot \mathbf{n}\,d\Omega$$
$$+ \int_{\Omega_H} \nabla \cdot (\boldsymbol{\sigma}_i \nabla \phi_m)w\,d\Omega = 0, \qquad (26)$$

where $\mathbf{n}$ is the unit outward normal.

Applying Green's theorem again to the second integral, we get

$$\int_{\Gamma_H} w[\boldsymbol{\sigma}_i + \boldsymbol{\sigma_e}]\nabla\phi_e \cdot \mathbf{n}\,d\Gamma - \int_{\Gamma_H} \phi_e[\boldsymbol{\sigma}_i + \boldsymbol{\sigma}_e]\nabla w \cdot \mathbf{n}\,d\Gamma$$
$$+ \int_{\Omega_H} \nabla \cdot ([\boldsymbol{\sigma}_i + \boldsymbol{\sigma}_e]\nabla w)\phi_e\,d\Omega$$
$$+ \int_{\Omega_H} \nabla \cdot (\boldsymbol{\sigma}_i \nabla \phi_m)w\,d\Omega = 0. \qquad (27)$$

This is the standard boundary integral equation for Poisson's equation with a general source term. For the special case of the source being given by $-\nabla \cdot (\boldsymbol{\sigma}_i \nabla \phi_m)$ this term can be transformed in a similar manner to the above, i.e.,

$$\int_{\Omega_H} \nabla \cdot (\boldsymbol{\sigma}_i \nabla \phi_m)w\,d\Omega$$
$$= \int_{\Gamma_H} w\boldsymbol{\sigma}_i \nabla \phi_m \cdot \mathbf{n}\,d\Gamma - \int_{\Omega_H} \boldsymbol{\sigma}_i \nabla \phi_m \cdot \nabla w\,d\Omega$$
$$= \int_{\Gamma_H} w\boldsymbol{\sigma}_i \nabla \phi_m \cdot \mathbf{n}\,d\Gamma - \int_{\Gamma_H} \phi_m \boldsymbol{\sigma}_i \nabla w \cdot \mathbf{n}\,d\Gamma$$
$$+ \int_{\Omega_H} \nabla \cdot (\boldsymbol{\sigma}_i \nabla w)\phi_m\,d\Omega. \qquad (28)$$

Inserting Eq. (28) into Eq. (27), we get

$$\int_{\Gamma_H} w[\boldsymbol{\sigma}_i + \boldsymbol{\sigma}_e]\nabla\phi_e \cdot \mathbf{n}\,d\Gamma - \int_{\Gamma_H} \phi_e[\boldsymbol{\sigma}_i + \boldsymbol{\sigma}_e]\nabla w \cdot \mathbf{n}\,d\Gamma$$
$$+ \int_{\Omega_H} \nabla \cdot ([\boldsymbol{\sigma}_i + \boldsymbol{\sigma}_e]\nabla w)\phi_e\,d\Omega$$
$$+ \int_{\Gamma_H} w\boldsymbol{\sigma}_i \nabla \phi_m \cdot \mathbf{n}\,d\Gamma - \int_{\Gamma_H} \phi_m \boldsymbol{\sigma}_i \nabla w \cdot \mathbf{n}\,d\Gamma$$
$$+ \int_{\Omega_H} \nabla \cdot (\boldsymbol{\sigma}_i \nabla w)\phi_m\,d\Omega = 0, \qquad (29)$$

which is a generalization of Eq. (31) from Yamashita.[34]

Equation (29) is general—no assumptions (apart from differentiability and integrability) have been made on w, $\boldsymbol{\sigma}_i$, or $\boldsymbol{\sigma}_e$. In the paper by Yamashita,[34] it was assumed that w was a Green's function satisfying

$$\nabla \cdot ([\boldsymbol{\sigma}_i + \boldsymbol{\sigma}_e]\nabla w) + \delta(\mathbf{x}_0) = 0 \qquad (30)$$

and

$$\boldsymbol{\sigma}_e \nabla w \cdot \mathbf{n} = 0 \quad \text{on} \quad \Gamma_B, \qquad (31)$$

where $\delta(\mathbf{x}_0)$ is the Dirac delta distribution centered at a point $\mathbf{x}_0$ within the torso and Γ_B is the surface of the torso. This resulted in the removal of the first volume integral in Eq. (29).

In practice, such a Green's function for the heart cannot be found analytically, since both $\boldsymbol{\sigma}_i$ and $\boldsymbol{\sigma}_e$ are in general anisotropic and inhomogeneous. If one assumes that they are homogeneous then both conductivity tensors can be represented by constant 3×3 matrices, which are diagonal in the coordinate system defined by the myocardial fibers and sheets. The fiber and sheet orientations in the heart are very complex and this anisotropy means that it is not possible to solve Eq. (30) analytically, even under the assumption of equal anisotropy ratios. This holds irrespective of whether we strive for a proper Green's function [i.e., impose Eq. (31)] or

merely look for a free-space Green's function (also known as a fundamental solution), which is a solution of Eq. (30) with appropriate boundary conditions at infinity (i.e., the no-flux condition on Γ_B is ignored).

If one assumes further that the heart domain is isotropic in both the extra and intracellular domains, then one can apply a standard boundary element procedure to Eq. (29). For this, we take w to be the free-space Green's function, i.e., a solution of

$$\nabla \cdot (\nabla w) + \delta(\mathbf{x}_0) = 0, \qquad (32)$$

where $\mathbf{x}_0$ is now an arbitrary point in space and w vanishes at infinity. In three dimensions, the solution of this equation is

$$w(\mathbf{x},\mathbf{x}_0) = \frac{1}{4\pi R}, \qquad (33)$$

where $R = \|\mathbf{r}\|_2 = \|\mathbf{x} - \mathbf{x}_0\|_2$ is the distance measured from $\mathbf{x}_0$.

With w defined as above, $\mathbf{x}_0$ inside Ω_H, and assuming material isotropy (i.e., $\boldsymbol{\sigma}_i = \sigma_i \mathbf{I}$, $\boldsymbol{\sigma}_e = \sigma_e \mathbf{I}$, and $\sigma_i = k\sigma_e$, where k is a constant), Eq. (32) can be used to simplify the domain integrals in Eq. (29), thus

$$\int_{\Omega_H} \nabla \cdot \{[\boldsymbol{\sigma}_i + \boldsymbol{\sigma}_e]\nabla w(\mathbf{x},\mathbf{x}_0)\}\phi_e(\mathbf{x})d\Omega(\mathbf{x})$$

$$= (1+k)\sigma_e \int_{\Omega_H} \nabla \cdot [\nabla w(\mathbf{x},\mathbf{x}_0)]\phi_e(\mathbf{x})d\Omega(\mathbf{x})$$

$$= -(1+k)\sigma_e\phi_e(\mathbf{x}_0), \qquad (34)$$

$$\int_{\Omega_H} \nabla \cdot [\boldsymbol{\sigma}_i \nabla w(\mathbf{x},\mathbf{x}_0)]\phi_m(\mathbf{x})d\Omega(\mathbf{x})$$

$$= k\sigma_e \int_{\Omega_H} \nabla \cdot [\nabla w(\mathbf{x},\mathbf{x}_0)]\phi_m(\mathbf{x})d\Omega(\mathbf{x})$$

$$= -k\sigma_e\phi_m(\mathbf{x}_0). \qquad (35)$$

Thus Eq. (29) becomes

$$(1+k)\sigma_e \int_{\Gamma_H} w(\mathbf{x},\mathbf{x}_0)\nabla\phi_e(\mathbf{x}) \cdot \mathbf{n}(\mathbf{x})d\Gamma(\mathbf{x})$$

$$-(1+k)\sigma_e \int_{\Gamma_H} \phi_e(\mathbf{x})\nabla w(\mathbf{x},\mathbf{x}_0) \cdot \mathbf{n}(\mathbf{x})d\Gamma(\mathbf{x})$$

$$-(1+k)\sigma_e\phi_e(\mathbf{x}_0) + k\sigma_e \int_{\Gamma_H} w(\mathbf{x},\mathbf{x}_0)\nabla\phi_m(\mathbf{x})$$

$$\cdot \mathbf{n}(\mathbf{x})d\Gamma(\mathbf{x}) - k\sigma_e \int_{\Gamma_H} \phi_m(\mathbf{x})\nabla w(\mathbf{x},\mathbf{x}_0)$$

$$\cdot \mathbf{n}(\mathbf{x})d\Gamma(\mathbf{x}) - k\sigma_e\phi_m(\mathbf{x}_0) = 0. \qquad (36)$$

The equation of more interest is the case when $\mathbf{x}_0 \in \Gamma_H$ (i.e., $\mathbf{x}_0$ on the boundary of the domain). To derive this equation, consider $\mathbf{x}_0$ at a smooth point on the boundary of Ω_H and construct a hemispherical region of radius ε centered at $\mathbf{x}_0$. Let Ω'_H be the extended region (i.e., Ω_H plus the hemispherical region). Then $\mathbf{x}_0$ is interior to Ω'_H so Eq. (36) is valid with Γ_H replaced by $\partial\Omega'_H$. One now considers this equation as $\lim_{\varepsilon\downarrow 0}$. If Γ_ε is the boundary of the hemispherical region, and $\Gamma_{-\varepsilon}$ the boundary of that part of Ω_H that is outside the hemisphere (so $\partial\Omega'_H = \Gamma_\varepsilon \cup \Gamma_{-\varepsilon}$), then we find that as long as the surface at $\mathbf{x}_0$ has a unique tangent plane,

$$\lim_{\varepsilon\downarrow 0}\int_{\Gamma_\varepsilon} \phi_e(\mathbf{x})\nabla w(\mathbf{x},\mathbf{x}_0) \cdot \mathbf{n}(\mathbf{x})d\Gamma(\mathbf{x})$$

$$= \lim_{\varepsilon\downarrow 0}\frac{-1}{4\pi R^2}2\pi R^2\phi_e(\boldsymbol{\gamma}) = -\frac{\phi_e(\mathbf{x}_0)}{2}, \qquad (37)$$

where $\boldsymbol{\gamma}$ is some point on the hemisphere of radius ε (the mean value theorem has been applied).

Similarly,

$$\lim_{\varepsilon\downarrow 0}\int_{\Gamma_\varepsilon} \phi_m(\mathbf{x})\nabla w(\mathbf{x},\mathbf{x}_0) \cdot \mathbf{n}(\mathbf{x})d\Gamma(\mathbf{x})$$

$$= \lim_{\varepsilon\downarrow 0}\frac{-1}{4\pi R^2}2\pi R^2\phi_m(\boldsymbol{\gamma}) = -\frac{\phi_m(\mathbf{x}_0)}{2}. \qquad (38)$$

It can also be shown that

$$\lim_{\varepsilon\downarrow 0}\int_{\Gamma_\varepsilon} w(\mathbf{x},\mathbf{x}_0)\nabla\phi_e(\mathbf{x}) \cdot \mathbf{n}(\mathbf{x})d\Gamma(\mathbf{x}) = 0 \qquad (39)$$

and

$$\lim_{\varepsilon\downarrow 0}\int_{\Gamma_\varepsilon} w(\mathbf{x},\mathbf{x}_0)\nabla\phi_m(\mathbf{x}) \cdot \mathbf{n}(\mathbf{x})d\Gamma(\mathbf{x}) = 0. \qquad (40)$$

As $\lim_{\varepsilon\downarrow 0}\Gamma_{-\varepsilon} \to \Gamma_H$ and, while the integrands are sin-

gular (when $\mathbf{x}_0$ is on Γ_H), the integrals exist in the standard sense, so one can write

$$\lim_{\varepsilon \downarrow 0} \int_{\Gamma_{-\varepsilon}} \text{(each integrand)} \ d\Gamma$$

$$= \int_{\Gamma_H} \text{(same integrand)} \ d\Gamma. \qquad (41)$$

Substituting Eqs. (37)–(41) into Eq. (36) and dividing through by $(1+k)\sigma_e$, we obtain the general boundary integral equation

$$c(\mathbf{x}_0)\phi_e(\mathbf{x}_0) + \int_{\Gamma_H} \phi_e(\mathbf{x})\nabla w(\mathbf{x},\mathbf{x}_0)\cdot\mathbf{n}(\mathbf{x})d\Gamma(\mathbf{x})$$

$$+ \frac{k}{1+k}c(\mathbf{x}_0)\phi_m(\mathbf{x}_0) + \frac{k}{1+k}$$

$$\times \int_{\Gamma_H} \phi_m(\mathbf{x})\nabla w(\mathbf{x},\mathbf{x}_0)\cdot\mathbf{n}(\mathbf{x})d\Gamma(\mathbf{x})$$

$$= \int_{\Gamma_H} \frac{w(\mathbf{x},\mathbf{x}_0)}{\sigma_i + \sigma_e}q_e(\mathbf{x})d\Gamma(\mathbf{x}) + \frac{k}{1+k}$$

$$\times \int_{\Gamma_H} w(\mathbf{x},\mathbf{x}_0)\nabla \phi_m(\mathbf{x})\cdot\mathbf{n}(\mathbf{x})d\Gamma(\mathbf{x}), \qquad (42)$$

where

$$c(\mathbf{x}_0) = \begin{cases} 1 & \text{if } \mathbf{x}_0 \in \Omega_H \\[2mm] \frac{1}{2} & \text{if } \mathbf{x}_0 \in \Gamma_H \text{ and } \Gamma_H \text{ smooth at } \mathbf{x}_0 \\[2mm] \dfrac{\text{internal solid angle}}{4\pi} & \text{if } \mathbf{x}_0 \in \Gamma_H \text{ and } \Gamma_H \text{ not smooth at } \mathbf{x}_0 \\[2mm] 0 & \text{if } \mathbf{x}_0 \text{ outside } \Omega_H \end{cases} \qquad (43)$$

and $q_e(\mathbf{x}) = \nabla\phi_e(\mathbf{x})\cdot\mathbf{n}(\mathbf{x})$ is the normal extracellular current at the point $\mathbf{x}$.

Equation (42) relates ϕ_e and ϕ_m at the point $\mathbf{x}_0$ to the values of ϕ_e, ϕ_m, q_e, and $\nabla\phi_m\cdot\mathbf{n}$ everywhere on Γ_H. On Γ_H, $\nabla\phi_m\cdot\mathbf{n}$ is 0 since transmembrane potentials are confined to the heart, which removes the last integral in Eq. (42).

Outside the heart, the torso potential, ϕ, is governed by

$$\nabla\cdot(\boldsymbol{\sigma}\nabla\phi) = 0, \qquad (44)$$

where $\boldsymbol{\sigma}$ is the conductivity of the passive torso tissues. This can be solved using a coupled finite-element/boundary-element procedure.[28] Continuity of (extracellular) potential and current across the myocardial boundaries provides the link between Eqs. (44) and (42). In the usual way, one can discretize the boundaries of all regions involved, and assemble the following matrices:

$$\begin{pmatrix} \text{all coefficients} \\ \text{of potentials from} \\ \text{Eq. (42)} \\ \text{and Eq. (44)} \end{pmatrix} \begin{pmatrix} \boldsymbol{\phi}_m \\ \boldsymbol{\phi}_e^H \\ \boldsymbol{\phi}^1 \\ . \\ . \\ . \\ \boldsymbol{\phi}^N \end{pmatrix}$$

$$= \begin{pmatrix} \text{all coefficients} \\ \text{of currents from} \\ \text{Eq. (42)} \\ \text{and Eq. (44)} \end{pmatrix} \begin{pmatrix} \mathbf{q}_e^H \\ \mathbf{q}^1 \\ . \\ . \\ . \\ \mathbf{q}^N \end{pmatrix}, \qquad (45)$$

where

N is the number of tissue regions outside the heart,

$\boldsymbol{\phi}^i$ is a vector of nodal values of ϕ in region i,

$\boldsymbol{\phi}_m$ is a vector of nodal values of ϕ_m on the heart,

$\boldsymbol{\phi}_e^H$ is a vector of nodal values of ϕ_e on the heart,

$\mathbf{q}^i$ is a vector of nodal values of q on the surface of region i, and

$\mathbf{q}_e^H$ is a vector of nodal values of q_e on the heart surface.

The coefficient matrices include all the continuity constraints. Also, since $\partial\phi_m/\partial\mathbf{n}$ is 0 on Γ_H, this term is

not present in Eq. (45). It is worth noting that the coefficients of ϕ_m in Eq. (42) are just $k/k+1$ times the coefficients of ϕ_e in that equation. Use of this fact allows one to speed up the assembly of Eq. (45).

APPENDIX B: ANALYTIC SOLUTION

From Fig. 1, we denote ϕ_e^{in} to be the potential inside the inner sphere and ϕ_e^{out} the potential between the inner and outer spheres. From Eq. (24) we have for $0 < r \leq R_1$,

$$\nabla^2 \left(\phi_e^{\text{in}} + \frac{\sigma_i}{\sigma_i + \sigma_e} \phi_m \right) = 0. \tag{46}$$

Now, in polar spheroidal coordinates, we chose ϕ_m to be the potential field generated by a centric dipole of magnitude $\boldsymbol{\rho} = (\rho_x, \rho_y, \rho_z)$ in rectangular Cartesian coordinates, inside a sphere of radius R_1 with a no-flux boundary condition at R_1, i.e.,

$$\phi_m(r, \theta, \zeta) = \frac{(R_1^3 + 2r^3)}{R_1^3 r^2} (\rho_x \cos \theta \sin \zeta + \rho_y \sin \theta \sin \zeta$$

$$+ \rho_z \cos \zeta). \tag{47}$$

Here, θ is the circumferential angle, ζ is the azithimuthal angle, and $P_n^m(\cos \zeta)$ is the associated Legendre polynomials of degree n and order m. With ϕ_m chosen, Eq. (13) is satisfied and ϕ_m is itself a solution to Laplace's equation inside the first sphere.

Thus, from Eq. (46) if ϕ_m is a solution to Laplace's equation, then we need to find ϕ_e^{in} such that $\phi_e^{\text{in}} - (\sigma_i/\sigma_i + \sigma_e) \phi_m$ satisfies Laplace's equation inside the first sphere. The general solution to Laplace's equation in polar spheroidal coordinates is

$$\phi_e^{\text{in}}(r, \theta, \zeta) = \sum_{n=0}^{\infty} \sum_{m=0}^{n} [A_{mn} \cos(m\theta) + B_{mn} \sin(m\theta)]$$

$$\times \left(C_{mn} r^n + \frac{D_{mn}}{r^{n+1}} \right) P_n^m(\cos \zeta). \tag{48}$$

From the orthogonality of spherical harmonic functions, we note that as our choice of ϕ_m only contains the $(0, 0)$, $(0, 1)$ and $(1,1)$ (m,n) coefficients, then the gen-

eral expression for ϕ_e^{in} must also only contain those coefficients, i.e.,

$$\phi_e^{\text{in}}(r, \theta, \zeta) = (A_{11} \cos \theta + B_{11} \sin \theta) \left(C_{11} r + \frac{D_{11}}{r^2} \right) \sin \zeta$$

$$+ A_{01} \left(C_{01} r + \frac{D_{01}}{r^2} \right) \cos \zeta + A_{00} \left(C_{00} + \frac{D_{00}}{r} \right)$$

$$- \frac{\sigma_i}{\sigma_i + \sigma_e} \phi_m(r, \theta, \zeta). \tag{49}$$

Grouping the coefficients

$$C_0 = A_{00} C_{00}, \quad C_1 = A_{01} C_{01},$$

$$D_0 = A_{00} D_{00}, \quad D_1 = A_{01} D_{01},$$

we obtain, for the inner sphere,

$$\phi_e^{\text{in}}(r, \theta, \zeta) = (A_{11} \cos \theta + B_{11} \sin \theta) \left(C_{11} r + \frac{D_{11}}{r^2} \right) \sin \zeta$$

$$+ \left(C_1 r + \frac{D_1}{r^2} \right) \cos \zeta + \left(C_0 + \frac{D_0}{r} \right)$$

$$- \frac{\sigma_i}{\sigma_i + \sigma_e} \phi_m(r, \theta, \zeta). \tag{50}$$

In the outer sphere Lapalace's equation must be satisfied for ϕ_e^{out}. From orthogonality of spherical harmonic functions, the general solution for the outside sphere is hence

$$\phi_e^{\text{out}}(r, \theta, \zeta) = (E_{11} \cos \theta + F_{11} \sin \theta) \left(G_{11} r + \frac{H_{11}}{r^2} \right) \sin \zeta$$

$$+ \left(G_1 r + \frac{H_1}{r^2} \right) \cos \zeta + \left(G_0 + \frac{H_0}{r} \right). \tag{51}$$

The resulting expressions for ϕ_e in the inner and outer spheres are hence

$$\phi_e(r,\theta,\zeta)$$

$$
= \begin{cases}
\left[(A_{11}\cos\theta + B_{11}\sin\theta)\left(C_{11}r + \dfrac{D_{11}}{r^2}\right)\sin\zeta + \left(C_1 r + \dfrac{D_1}{r^2}\right)\cos\zeta + C_0 + \dfrac{D_0}{r} - \dfrac{\sigma_i}{\sigma_i + \sigma_e}\right]\phi_m(r,\theta,\zeta) & 0 < r \leqslant R_1, \\[4mm]
(E_{11}\cos\theta + F_{11}\sin\theta)\left(G_{11}r + \dfrac{H_{11}}{r^2}\right)\sin\zeta + \left(G_1 r + \dfrac{H_1}{r^2}\right)\cos\zeta + G_0 + \dfrac{H_0}{r} & R_1 < r \leqslant R_2.
\end{cases}
\tag{52}
$$

Substituting Eq. (52) into Eq. (14), we find that continuity of potential across the inner sphere boundary implies

$$G_0 + \frac{H_0}{R_1} = C_0 + \frac{D_0}{R_1}, \tag{53}$$

$$E_{11}\left(G_{11}R_1 + \frac{H_{11}}{R_1^2}\right) = A_{11}\left(C_{11}R_1 + \frac{D_{11}}{R_1^2}\right)$$
$$- \frac{3\sigma_i}{R_1^2(\sigma_i + \sigma_e)}\rho_x, \tag{54}$$

$$F_{11}\left(G_{11}R_1 + \frac{H_{11}}{R_1^2}\right) = B_{11}\left(C_{11}R_1 + \frac{D_{11}}{R_1^2}\right)$$
$$- \frac{3\sigma_i}{R_1^2(\sigma_i + \sigma_e)}\rho_y, \tag{55}$$

$$G_1 R_1 + \frac{H_1}{R_1^2} = C_1 R_1 + \frac{D_1}{R_1^2} - \frac{3\sigma_i}{R_1^2(\sigma_i + \sigma_e)}\rho_z. \tag{56}$$

Substituting Eq. (52) into Eq. (15), we find that continuity of current across the inner sphere boundary implies

$$\frac{\sigma H_0}{R_1^2} = \frac{(\sigma_i + \sigma_e)D_0}{R_1^2}, \tag{57}$$

$$\sigma E_{11}\left(G_{11} - \frac{2H_{11}}{R_1^3}\right) = (\sigma_i + \sigma_e)A_{11}\left(C_{11} - \frac{2D_{11}}{R_1^3}\right), \tag{58}$$

$$\sigma F_{11}\left(G_{11} - \frac{2H_{11}}{R_1^3}\right) = (\sigma_i + \sigma_e)B_{11}\left(C_{11} - \frac{2D_{11}}{R_1^3}\right), \tag{59}$$

$$\sigma\left(G_1 - \frac{2H_1}{R_1^3}\right) = (\sigma_i + \sigma_e)\left(C_1 - \frac{2D_1}{R_1^3}\right). \tag{60}$$

Substituting Eq. (52) into Eq. (16), we find that no flux across the outer sphere implies

$$G_{11} - \frac{2H_{11}}{R_2^3} = 0, \tag{61}$$

$$G_1 - \frac{2H_1}{R_2^3} = 0, \tag{62}$$

$$-\frac{H_0}{R_2^2} = 0. \tag{63}$$

Substituting Eq. (52) into Eq. (17), we find that specification of a reference potential at the top of the outer sphere implies

$$G_1 R_1 + \frac{H_1}{R_2^2} + G_0 + \frac{H_0}{R_2} = \phi_{\text{ref}}. \tag{64}$$

Equations (53)–(64) form two independent sets of linear equations. The first set contains Eqs. (54), (55), (58), (59), and (61), which involve the eight unknowns A_{11}, B_{11}, C_{11}, D_{11}, E_{11}, F_{11}, G_{11}, and H_{11}. The second set contains Eqs. (53), (56), (57), (60), and (62)–(64), which involves the eight unknowns C_0, C_1, D_0, D_1, G_0, G_1, H_0, and H_1.

To solve the first set of equations, three of the eight unknown coefficients must be fixed. When selecting the coefficients to fix, it should be noted that both G_{11} and H_{11} cannot be fixed together, since they are related through Eq. (61). Because it is desirable to have the resultant circumferential variation directly dependent on the underlying dipole orientation that is generating ϕ_m, the C_{11}, D_{11}, and H_{11} coefficients were chosen so as to normalize the equations in the radial direction. With these three coefficients fixed, we obtain from Eq. (61),

$$G_{11} = \frac{2H_{11}}{R_2^3}. \tag{65}$$

From Eqs. (58) and (59), we find

$$E_{11} = \frac{(\sigma_i + \sigma_e)R_2^3(R_1^3 C_{11} - 2D_{11})}{2\sigma(R_1^3 - R_2^3)H_{11}} A_{11} = \alpha A_{11}, \quad (66)$$

$$F_{11} = \frac{(\sigma_i + \sigma_e)R_2^3(R_1^3 C_{11} - 2D_{11})}{2\sigma(R_1^3 - R_2^3)H_{11}} B_{11} = \alpha B_{11}, \quad (67)$$

and thus from Eqs. (54) and (55) we obtain

$$A_{11} = \frac{-3\sigma_i R_2^3}{(\sigma_i + \sigma_e)[\alpha(2R_1^3 + R_2^3)H_{11} - R_2^3(C_{11}R_1^3 + D_{11})]} \rho_x$$
$$= \beta \rho_x, \quad (68)$$

$$B_{11} = \frac{-3\sigma_i R_2^3}{(\sigma_i + \sigma_e)[\alpha(2R_1^3 + R_2^3)H_{11} - R_2^3(C_{11}R_1^3 + D_{11})]} \rho_y$$
$$= \beta \rho_y. \quad (69)$$

To solve the second set of equations, one of the unknown eight coefficients must be fixed. In choosing the coefficient it should be noted that H_0 [and thus D_0 from Eq. (57)] cannot be fixed since it is implicitly zero from Eq. (63). It should also be noted that if C_0 or G_0 is fixed the resulting expression for ϕ_e in the outer sphere will not depend on the dipole source generating ϕ_m. For this reason, and to be consistent with the choice of coefficients from the first set of equations, C_1 is the coefficient chosen to be fixed. Thus, from Eq. (63), we find that $H_0 = 0$ and therefore $D_0 = 0$ from Eq. (57). This gives $C_0 = G_0$ from Eq. (53).

From Eq. (62) we have

$$G_1 = \frac{2H_1}{R_2^3}, \quad (70)$$

and thus from Eqs. (56) and (60), we obtain

$$D_1 = \frac{3(2R_1^3 + R_2^3)((\sigma_i + \sigma_e)R_1^2 C_1 - 2\sigma_i \rho_z)}{2[(2\sigma_i + 2\sigma_e + \sigma)R_1^3 + (\sigma_i + \sigma_e - \sigma)R_2^3]} - R_1^3 C_1$$
$$+ \frac{3\sigma_i \rho_z}{\sigma_i + \sigma_e} \quad (71)$$

and

$$H_1 = \frac{3R_2^3[(\sigma_i + \sigma_e)R_1^3 C_1 - 2\sigma_i \rho_z]}{2[(2\sigma_i + 2\sigma_e + \sigma)R_1^3 + (\sigma_i + \sigma_e - \sigma)R_2^3]}. \quad (72)$$

The final coefficient can then be obtained from Eq. (64), i.e.,

$$G_0 = \phi_{\text{ref}} - \frac{9R_2[(\sigma_i + \sigma_e)R_1^3 C_1 - 2\sigma_i \rho_z]}{2[(2\sigma_i + 2\sigma_e + \sigma)R_1^3 + (\sigma_i + \sigma_e - \sigma)R_2^3]}. \quad (73)$$

To obtain a particular solution for numerical testing, we chose $R_1 = 1$ and $R_2 = 3$, $\boldsymbol{\rho} = (1,2,1)$, $\sigma_i = 2$, $\sigma_e = 4$, $\sigma = 2$, $C_{11} = 1$, $D_{11} = 1$, $H_{11} = 1$, $C_1 = 1$, and $\phi_{\text{ref}} = 0$. The full set of 16 coefficients for this particular case is given by

$$A_{11} = \frac{52}{17}, \quad E_{11} = \frac{81}{17},$$

$$B_{11} = \frac{104}{17}, \quad F_{11} = \frac{162}{17},$$

$$C_{11} = 1, \quad G_{11} = \frac{2}{27},$$

$$D_{11} = 1 \quad H_{11} = 1,$$

$$C_1 = 1, \quad G_1 = \frac{3}{61},$$

$$D_1 = \frac{87}{122}, \quad H_1 = \frac{81}{122},$$

$$C_0 = \frac{-27}{122}, \quad G_0 = \frac{-27}{122},$$

$$D_0 = 0, \quad H_0 = 0.$$

The final expressions for the extracellular potential and normal current for this particular case are given by Eqs. (18) and (19).

It should be noted that both ϕ_m and ϕ_e^{in} contain a $1/r^2$ singularity at $r = 0$. The effect of this singularity must be taken into account when performing an integration of the type in Eq. (25). Because of the form of ϕ_e^{in}, the singularity from ϕ_m cancels out. The resulting singularity from ϕ_e^{in} acts like a dipole source when integrated with the weighting function. The correction factor that hence needs to be added to the left-hand side of Eq. (42) is

$$4\pi \boldsymbol{\rho}^* \cdot \nabla w(\boldsymbol{\rho}_0^*, \mathbf{x}_0) = \frac{\boldsymbol{\rho}^* \cdot \mathbf{r}}{R^3}, \quad (74)$$

where $\rho^* = (A_{11}D_{11}, B_{11}D_{11}, D_1)$ is the pseudodipole singularity source, $\rho_0^* \equiv 0$ is the location of the singularity, and $w(\rho_0^*, \mathbf{x}_0)$ is the free-space Green's function defined by Eq. (33).

REFERENCES

[1] Barr, R. C., and M. S. Spach. Inverse calculation of QRS-T epicardial potentials from body surface potential distributions for normal and ectopic beats in the intact dog. *Circ. Res.* 42:661–675, 1978.

[2] Bradley, C. P. A three-dimensional torso model for electrocardiology. PhD thesis, The University of Auckland, New Zealand, 1998.

[3] Bradley, C. P., M. P. Nash, L. K. Cheng, A. J. Pullan, and D. J. Paterson. Electrocardiographic inverse validation study: Model development and methodology. *FASEB J.* 14:A442, 2000.

[4] Bradley, C. P., A. J. Pullan, and P. J. Hunter. Geometric modeling of the human torso using cubic Hermite elements. *Ann. Biomed. Eng.* 25:96–111, 1997.

[5] Bradley, C. P., A. J. Pullan, and P. J. Hunter. Effects of material properties and geometry on electrocardiographic forward simulations. *Ann. Biomed. Eng.* 28:721–741, 2000.

[6] Buist, M., and A. Pullan. From cell to body surface: A fully coupled approach. J. Electrocardiol. (in press).

[7] Cheng, L. K., and A. J. Pullan. Towards noninvasive electrical heart imaging. In: Proceedings of the First Joint Meeting of BMES & IEEE/EMBS. Atlanta, GA, October 1999, p. 57.

[8] Cuppen, J., and A. van Oosterom. Model studies with the inversely calculated isochrones of ventricular depolarization. *IEEE Trans. Biomed. Eng.* 31:652–659, 1984.

[9] Fischer, G., B. Tilg, P. Wach, R. Modre, U. Leder, and H. Nowak. Application of high-order boundary elements to the electrocardiographic inverse problem. *Comput. Methods Programs Biomed.* 58:119–131, 1999.

[10] Foster, K. R., and H. P. Schwan. Dielectric properties of tissue and biological materials: A critical review. *Crit. Rev. Biomed. Eng.* 17:25–104, 1989.

[11] Geddes, L. A., and L. E. Baker. The specific resistance of biological material—a compendium of data for the biomedical engineer and physiologist. *Med. Biol. Eng.* 5:271–293, 1967.

[12] Green, L. S., B. Taccardi, P. R. Ershler, and R. L. Lux. Effects of conducting media on isopotential and isochrone distributions. *Circulation* 84:2513–2521, 1991.

[13] Greensite, F. Remote reconstruction of confined wave-front propagation. *Inverse Probl.* 11:361–370, 1995.

[14] Greensite, F. Computational Inverse Problems in Electrocardiography. Southampton, U.K.: WIT Press, 2001, Chap. 3.

[15] Greensite, F., and G. Huiskamp. An improved method for estimating epicardial potentials from the body surface. *IEEE Trans. Biomed. Eng.* 45:98–104, 1998.

[16] Gulrajani, R. M., F. A. Roberge, and P. Savard. Moving dipole inverse ECG and EEG solutions. *IEEE Trans. Biomed. Eng.* 31:903–910, 1984.

[17] Huiskamp, G., and F. Greensite. A new method for myocardial activation imaging. *IEEE Trans. Biomed. Eng.* 44:433–446, 1997.

[18] Huiskamp, G. J., and A. van Oosterom. The depolarization sequence of the human heart surface computed from measured body surface potentials. *IEEE Trans. Biomed. Eng.* 35:1047–1059, 1988.

[19] Le Grice, I. J., P. J. Hunter, and B. H. Smaill. Laminar structure of the heart: A mathematical model. *Am. J. Physiol.* 272:H2466–H2476, 1997.

[20] Martin, R. O., T. C. Pilkington, and M. Morrow. Statistically constrained inverse electrocardiography. *IEEE Trans. Biomed. Eng.* 22:487–492, 1975.

[21] Nash, M. P., C. P. Bradley, L. K. Cheng, A. J. Pullan, and D. J. Paterson. Electrocardiographic inverse validation study: *In vivo* mapping and analysis. *FASEB J.* 14:A442, 2000.

[22] Nash, M. P., C. P. Bradley, L. K. Cheng, A. J. Pullan, and D. J. Paterson. An experimental–computational framework for validating *in vivo* ECG inverse algorithm. *Intl. J. Bioelectromagn.* 2, 2000.

[23] Nash, M. P., C. P. Bradley, A. Kardos, A. J. Pullan, and D. J. Paterson. An experimental model to correlate simultaneous body surface and epicardial electropotential recordings *in vivo*. *Chaos, Solitons Fractals* (in press).

[24] Nielsen, P. M. F., I. J. Le Grice, B. H. Smaill, and P. J. Hunter. Mathematical model of geometry and fibrous structure of the heart. *Am. J. Physiol.* 260:H1365–H1378, 1991.

[25] Oster, H., and Y. Rudy. The use of temporal information in the regularization of the inverse problem of electrocardiography. *IEEE Trans. Biomed. Eng.* 39:65–75, 1992.

[26] Oster, H., B. Taccardi, R. Lux, P. Ershler, and Y. Rudy. Noninvasive electrocardiographic imaging. Reconstruction of epicardial potentials, electrograms, and isochrones and localization of single and multiple electrocardiac events. *Circulation* 96:1012–1024, 1997.

[27] Oster, H., B. Taccardi, R. Lux, P. Ershler, and Y. Rudy. Electrocardiographic imaging. Noninvasive characterization of intramural myocardial activation from inverse-reconstructed epicardial potentials and electrograms. *Circulation* 97:1496–1507, 1998.

[28] Pullan, A. J. A high-order coupled finite-element/boundary-element torso model. *IEEE Trans. Biomed. Eng.* 43:292–298, 1996.

[29] Pullan, A. J., L. K. Cheng, M. P. Nash, and D. J. Paterson. Noninvasive electrical imaging of the heart. In: Proceedings of the First Joint Meeting of BMES & IEEE/EMBS. Atlanta, GA, October 1999, p. 191.

[30] Rush, S., J. A. Abildskov, and R. McFee. Resistivity of body tissues at low frequencies. *Circ. Res.* 12:40–50, 1963.

[31] Spach, M. S., W. T. Miller III, E. Miller-Jones, R. B. Warren, and R. C. Barr. Extracellular potentials related to intracellular potentials during impulse conduction in anisotropic cardiac muscle. *Circ. Res.* 45:188–204, 1979.

[32] Tikhonov, A., and V. Arsenin. Solution of Ill-Posed Problems. Washington, DC: Wiley, 1977.

[33] Tomlinson, K. A. Finite element solution of an eikonal equation for excitation wavefront propagation in ventricular myocardium. PhD thesis, The University of Auckland, New Zealand, 2000.

[34] Yamashita, Y., and D. Geselowitz. Source-field relationships for cardiac generators on the heart surface based on their transfer coefficients. *IEEE Trans. Biomed. Eng.* 32:964–970, 1985.